Article:

De Luca, F, Menzel, R, Blaker, JJ et al. (3 more authors) (2015) Nacre-nanomimetics: Strong, Stiff & Plastic. ACS Applied Materials and Interfaces, 7 (48). pp. 26783-26791. ISSN 1944-8252

https://doi.org/10.1021/acsami.5b08838

Nacre-nanomimetics: Strong, Stiff & Plastic

Francois De Luca[1], Robert Menzel[2], Jonny J. Blaker[1]†, John Birkbeck[2], Alexander Bismarck[1], Milo S. P. Shaffer[2*]

[1] Polymer & Composite Engineering (PaCE) Group, Department of Chemical Engineering,
[2]Department of Chemistry, Imperial College London, South Kensington Campus, London SW7 2AZ, UK

[*]Address correspondence to m.shaffer@imperial.ac.uk

Keywords*:* *Nacre-nanomimetic, Layer-by-Layer assembly, mechanical properties*, *in-situ characterization, "brick-and-mortar" arrangement, deformation mechanisms, plastic deformation*

Abstract: The bricks and mortar in the classic structure of nacre have characteristic geometry, aspect ratios and relative proportions; these key parameters can be retained whilst scaling down the absolute length scale by more than one order of magnitude. The results shed light on fundamental scaling behavior and provide new opportunities for high performance, yet ductile, lightweight nanocomposites. Reproducing the toughening mechanisms of nacre at smaller length scales allows a greater volume of interface per unit volume whilst simultaneously increasing the intrinsic properties of the inorganic constituents. Layer-by-Layer (LbL) assembly of poly (sodium 4-styrene sulfonate) (PSS) polyelectrolyte and well-defined $[Mg_2Al(OH)_6]CO_3.nH_2O$ layered double hydroxide (LDH) platelets produces a dense, oriented, high inorganic content (~90 wt%) nanostructure resembling natural nacre, but at a shorter length scale. The smaller building blocks enable the (self-) assembly of a higher quality nanostructure than conventional mimics, leading to improved mechanical properties, approaching those of natural nacre, whilst allowing for substantial plastic deformation. Both strain hardening and crack deflection mechanisms were observed *in situ* by scanning electron microscopy (SEM) during nanoindentation. The best properties emerge from an ordered nanostructure, generated using regular platelets, with narrow size dispersion.

Introduction

Like many natural composites, the structure of nacre, found in the inner part of some mollusk shells, is a complex hierarchical structure organized over multiple hierarchical levels leading to coupled toughening mechanisms.[1-6] In particular, its characteristic "brick-and-mortar" structure[7] is understood to play the key role in developing a high resistance to defects; it consists of 95 % brittle inorganic aragonite ($CaCO_3$) building blocks, around 200-900 nm thick and 5-8 µm wide (aspect ratio from 7-15),[8] "glued" together by a soft chitin-containing organic framework. This organic layer is around 20-30 nm thick[9] and makes up the remaining 5 % of the structure. The combination of a small fraction of organic phase along with this specific three-dimensional architecture leads to exceptional mechanical properties, including high toughness (≈ 1.24 kJ.m^{-2}), strength (≈ 140 MPa) and stiffness (E ≈ 60 GPa).[10,11] When loaded, the "bricks" have the ability to slide over one another within the organic phase and eventually interlock[12,13] via a range of possible mechanisms,[14] leading to strain hardening.[14,15] In addition, when a crack initiates from a defect within the nacre structure, multiple crack deflections occur at the building block interfaces.[16]

According to the Griffith criterion, the fracture strength of pure aragonite platelets can be optimized by reducing their thickness to less than 30 nm.[17] In natural nacre, the platelets are up to an order of magnitude thicker than the critical thickness, h*, below which a material becomes flaw-tolerant.[2,17,18] The relatively large dimensions of the platelets contained in nacre may be limited by either the thickness of a single biopolymer molecule, which is already close to 20 nm spacing between the platelets[14,19,20] or the scale of cell-driven mineralization. On the other hand, the larger thickness of the natural platelets is likely mitigated by their internal structure, since they are not pure mineral, but a nanocomposite of mineral grains in a secondary matrix.[3-5,21] Nevertheless, many models[7,10,17,18,22-24] have been developed to understand and, therefore, reproduce the mechanical performance of the primary "brick-and-mortar" structure of nacre, specifically the combination of high strength, stiffness and toughness. The aspect ratio of the platelets has been identified as a critical parameter.[7,22-24] High stiffness and high strength are achieved by increasing platelet anisotropy.[18,22] However, the toughening mechanisms of nacre only occur below a critical aspect ratio, which allows pull-out and subsequent sliding of the platelets.[25,26] Whilst the characteristic toughening mechanisms of nacre are expected to be scale invariant,[23,24] the models predict that the best nacre mimics should be achieved with small platelets at the optimum critical aspect ratio.[22-24] Therefore, it is of great interest to consider whether the performance might be improved by reproducing the geometry of natural nacre at reduced absolute length scale. A higher platelet interface volume fraction may enable plasticity and toughening as the process zone toughening could be significantly increased by the reduction of platelet thickness.[22,23] In addition, given the difficulty of synthesizing a controlled secondary grain structure, shrinking the platelets to less than the critical flaw size should be advantageous.

The structure of nacre has motivated many researchers to design lightweight composites with superior mechanical properties.[27,28] The production of mimics at the natural nacre length scale, using dip coating techniques,[26,29] typically incorporates relatively low volume fractions of inorganic platelets due to platelet misalignment, limiting the mechanical performance. On the other hand, exfoliated nanosheets of LDH,[30] montmorillonite clay[31-35] and graphene oxide[36-41] with a high aspect ratio (>200) have been used to generate layered hybrids containing nanometer-thickness platelets. Although oriented to the plane, the structures tend to have significant nanosheet overlap and inhomogeneous exfoliation; at nanosheet contents higher than 70 wt.%, the structures become influenced by tactoid formation,[42] limiting the assembly of a homogeneous "brick-and-mortar" arrangement to low reinforcement fractions. In these systems, the platelet thickness is reduced excessively to less than or similar to the polymer binder thickness, yielding hybrids with a significantly greater organic content than nacre.

The use of well-defined discrete LDH nanoplatelets, with an aspect ratio similar to the aragonite platelets in nacre, offers an alternative; an intermediate absolute platelet thickness in the range 10-20 nm, can be combined with a simple polymer organic 'mortar' around ten times thinner than the natural biopolymer, such that the correct dimensional ratios and phase proportions can be retained. LDH was selected due to the availability of stable dispersions of near monodispersed, individualized nanoplatelets, with the desired dimensions, and a high surface charge, enabling assembly with a suitable, complementary, soft polyelectrolyte (PSS). The Layer-by-Layer (LbL) assembly method was then used to deposit well-controlled alternating layers, allowing the alignment of anisotropic nanoplatelets by simple sequential dipping.[43] The approach assembles a more effective mimic of the primary brick-and-mortar structure, at a new lengthscale, which may obviate the need for internal platelet hierarchy.

Results and discussion

$[Mg_2Al(OH)_6]CO_3$-$n$$H_2O$ LDH platelets were synthesized by co-precipitation, followed by hydrothermal treatment[44] at various conditions. The hydrothermal treatment converted the amorphous slurry of LDH, obtained after co-precipitation of the metal salt with base, to individual, highly crystalline particles. The TEM images (Fig.S1, supplementary information) also confirmed that the products formed stable individualized dispersions in aqueous solution, as required for successful monolayer deposition via LbL assembly. Positively-charged LDH platelets (zeta-potential shown in Fig. S3, supplementary information) in water (diluted to 0.3 wt%, at pH 10) formed stable electrostatically-stabilized colloids with agglomeration visible only after several months storage at room temperature. Three different conditions were used to synthesize LDH platelets with different dimensions and polydispersity (Tab. 1), to explore the effects on assembly and mechanical properties. The average diameter and diameter distributions of the synthesized LDH platelets were determined from Transmission Electron Microscopy (TEM) images (Fig. S1, supplementary information); the thickness was also measured via TEM images of edge-on platelets (Fig. S1, supplementary information) but more accurately determined using the Scherrer broadening of the (003) X-ray diffraction peak (Fig. S2, supplementary information); both methods led to similar values. All the platelets had a mean aspect ratio between 6 and 10 (Tab. 1), similar to the natural aragonite in nacre[8]. Hydrothermal treatment at 100 °C for 4 h and 72 h, produced narrow particle size distributions, with means ~50 nm (LDH-1) and ~130 nm (LDH-2), respectively. After 72 h at 125 °C, the mean diameter remained around ~130 nm but with much greater polydispersity (LDH-3).

LbL coatings successfully formed on consecutive immersion of a quartz or glass slide into an aqueous LDH platelet dispersions and a PSS solution; rinsing in pure water after each dipping step removed excess particles to yield monolayers consistently (Fig. S4, supplementary information). Regular multilayer coatings were formed using an automated dipping robot, and monitored by UV-Vis spectroscopy (Fig. S5, supplementary information). The absorbance band at 225 nm is related to the phenyl group of PSS,[45] whilst the broad scattering feature is attributed to the platelets. Both features increased linearly (Fig. 1.A and Fig. 1.B) with increasing number (n) of deposited bilayers, confirming good thickness control. Linear slopes for the 225 nm peak indicate that a similar amount of PSS was added during each deposition cycle, regardless of platelet type. The thickness of the PSS monolayer is expected[46] to be around 1 nm, significantly thinner than that of LDH.

The consistent appearance of the optical interference color generated by the films (Fig. 1.C) indicates excellent uniformity. Even the thickest $(LDH/PSS)_n/LDH$ coatings retained a uniform, densely-packed final layer as imaged by SEM (Fig. 1.D-I); cross-sections (Fig. 1.G-I) show homogenous coatings with thicknesses of ~1 µm for both $(LDH\text{-}1/PSS)_{155}/LDH\text{-}1$ and $(LDH\text{-}2/PSS)_{50}/LDH\text{-}2$ and ~1.3 µm for $(LDH\text{-}3/PSS)_{50}/LDH\text{-}3$. The quality of the platelet alignment after the deposition of so many bilayers, especially for the $(LDH\text{-}2/PSS)_{50}/LDH\text{-}2$ coating, is a significant improvement compared to other artificial nacre coatings made of inorganic nanosheets[31] or µm-large inorganic platelets.[26]

The degree of alignment was quantified using three-dimensional X-ray Diffraction (XRD) rocking curves, acquired at a fixed $2\theta=11.7°$, corresponding to the (003) interlayer reflexion parallel to the LDH platelet surface. Misalignment values were obtained from the Full Width at Half Maximum (FWHM) of the rocking curves (Fig. 2.B and Fig. S6, supplementary information). The LDH platelets in the $(LDH\text{-}2/PSS)_{50}/LDH\text{-}2$ coating showed an encouragingly high degree of alignment (±8°). Nacre mimics at a natural length scale (produced by Bonderer et al.[26]) also led a platelet misalignment of about 8°, with an inorganic content of 70 vol%. An alignment value of about ±15° has been reported for the systems containing 50 wt% of ~1 nm thick clay nanosheets[35] with an aspect ratio of 25. Greater LDH polydispersity and higher numbers of deposited bilayers reduced the alignment quality of the $(LDH\text{-}3/PSS)_{50}/LDH\text{-}3$ (±17°) and $(LDH\text{-}1/PSS)_{155}/LDH\text{-}1$ (±20°) coatings, respectively. In dense films, poorer alignment should correlate with an increase in organic content, as in fact confirmed by Thermal Gravimetric Analysis (Tab. 1 and Fig. S7, supplementary information). The most ordered $(LDH\text{-}2/PSS)_{50}/LDH\text{-}2$

reached an inorganic content of 88.4 wt.%, approaching that of natural nacre (~95 wt.%). The two other coatings [$(LDH\text{-}1/PSS)_{155}/LDH\text{-}1$ and $(LDH\text{-}3/PSS)_{50}/LDH\text{-}3$] exhibited an inorganic content of 57.3 and 83.3 %, respectively (Tab. 1). In addition to good platelet alignment and low organic content, the $(LDH\text{-}2/PSS)_{50}/LDH\text{-}2$ coating has a high degree of packing with a "brick-and-mortar" appearance as exemplified by TEM cross sections mapped using EDX to distinguish the LDH platelets from the polymer (Fig. 2), similar to the randomly platelet-distributed "sheet nacre" structure found in bivalves[47] (*Nucula nitidosa*). The carbon atoms contained in the PSS layer are well distributed around the platelets, which themselves have a uniform composition of Mg/Al/O.

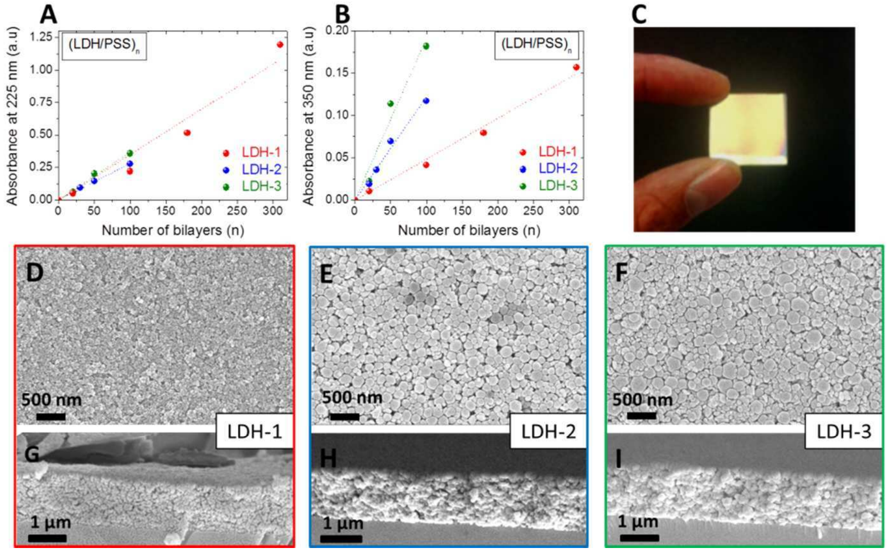

Figure 1. Layer-by-Layer assembly of $(LDH/PSS)_n/LDH$ multilayer coatings with different inorganic platelets dimensions and size distribution leading to varying organic content. Layer-by-Layer assembly of $(LDH/PSS)_n/LDH$ coatings monitored by UV-Vis absorbance values at 225 nm (PSS absorption) and 350 nm (scattering) from deconvoluted UV-Vis spectra (A and B, respectively). Photograph of µm-thick $(LDH\text{-}2/PSS)_{50}/LDH\text{-}2$ coating deposited on glass slide with high uniformity (C). SEM top and cross section images of $(LDH\text{-}1/PSS)_{155}/LDH\text{-}1$ (D and G), $(LDH\text{-}2/PSS)_{50}/LDH\text{-}2$ (E and H) and $(LDH\text{-}3/PSS)_{50}/LDH\text{-}3$ (F and I) coatings.

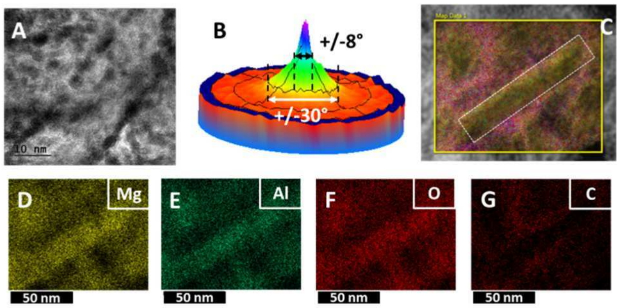

Figure 2. "Brick-and-mortar" $(LDH/PSS)_n/LDH$ nanostructures. TEM image of $(LDH\text{-}2/PSS)_n/LDH\text{-}2$ cross section (A). Three-dimensional rocking curves of (LDH-2/PSS)n/LDH-2 coating (B) acquired for 2θ=11.7°, Ψ=[0;80°] (graph step: 30°) and Φ=[0;360°] (graph step: 90°). EDX mapping acquired during TEM cross-sectional imaging of $(LDH\text{-}2/PSS)_{50}/LDH\text{-}2$ nanostructure (C), with Mg, Al, O and C atom distributions (D, E, F and G, respectively).

The mechanical properties of the different coatings deposited on quartz substrates were determined by nanoindentation (Tab. 2). Similarly to natural nacre interlayers, the behavior of the soft, hydroscopic phase is humidity dependent, so the samples were conditioned and tested under controlled relative humidity. By TGA, all coatings contained about or less than 5 % water (Fig S.7, supplementary information). Elastic modulus and hardness of the coatings were determined from the unloading segment of the load-displacement curves (Fig. 3.A-C) using the Oliver and Pharr method.[48] Although this approach strictly assumes a homogenous system, it has been widely applied to evaluate artificial nacre with both micro-[49] and nano-reinforcement.[50] In shallow indentations, particularly with sharp tips, results are strongly influenced by the intrinsic platelet properties, including the secondary grain structure.[6]

However, with increasing depth, the elastic modulus and hardness measured for natural nacre progressively decrease, reaching a plateau beyond one platelet thickness, presumably related to the properties of the whole structure.[51] A similar value for hardness (~2.5 GPa) was obtained[52] by Vickers indentation of natural nacre to a depth of about 3 µm. Therefore, the different $(LDH\text{-}x/PSS)_n/LDH\text{-}x$ coatings were indented to a depth of several platelet thicknesses, to compare with equivalent data for natural nacre. The plastic and elastic works of indentation were assessed from the area under the corresponding segments of the load-displacement curves. $(LDH\text{-}2/PSS)_n/LDH\text{-}2$ provided the highest modulus (65.8 ± 3.2 GPa) of the samples and indeed the highest value measured for any artificial nacre via nanoindentation; the result highlights the importance of producing nacre nanocomposites with high inorganic content and a well-organized uniform nanostructure. Despite the similarly high platelet content, $(LDH\text{-}3/PSS)_n/LDH\text{-}3$ possessed a lower modulus with greater scatter due to the heterogeneity in the structure; the lower modulus of $(LDH\text{-}1/PSS)_n/LDH\text{-}1$ is due to the higher loading of organic phase content. Similar trends were observed in hardness, again the $(LDH\text{-}2/PSS)_n/LDH\text{-}2$ coating performs best (2.34 ± 0.18 GPa). The mechanical properties are similar to natural nacre, which according to comparable nanoindentation data, has an elastic modulus and hardness of about 50-60 GPa and 2-3 GPa, respectively.[51] Shallow indenation of natural nacre indicated slightly higher values, around 60-70 GPa and 3-4 GPa, respectively.[21,53] The layer thickness ratio of the $(LDH\text{-}2/PSS)_n/LDH\text{-}2$ coating was estimated to be 13.6, which is similar to that of natural nacre and close to the optimum value of about 10 found for nanocomposites of alternating continuous TiO_2 nanoparticle and polyelectrolyte layers.[54] The elastic modulus and hardness of all nacre-nanometic coatings are expected to decrease with an increase in water content, as observed for both PVA/nanoclay-based nacre mimics[35] and natural nacre (wet and dry elastic modulus of 60 and 70 GPa, repectively).[20]

Table.1 Properties of treated LDH platelets and characteristics of a comparative sub-set of $(LDH/PSS)_n/LDH$ artificial nacre coatings

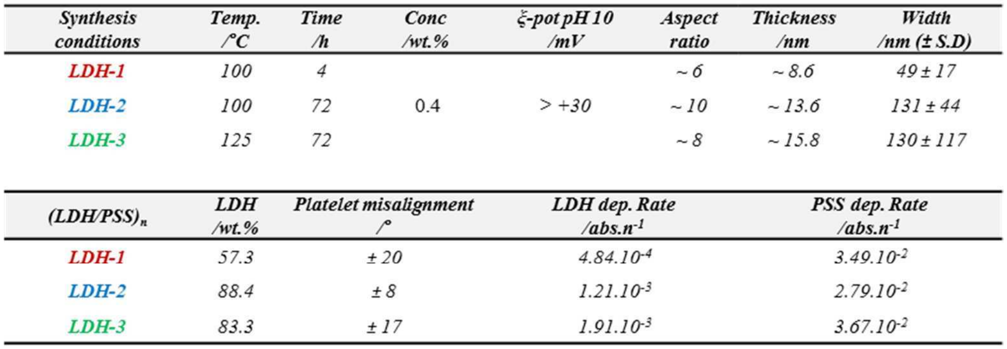

Synthesis conditions	*Temp. /°C*	*Time /h*	*Conc /wt.%*	*ξ-pot pH 10 /mV*	*Aspect ratio*	*Thickness /nm*	*Width /nm (± S.D)*
LDH-1	100	4	0.4	> +30	~ 6	~ 8.6	49 ± 17
LDH-2	100	72			~ 10	~ 13.6	131 ± 44
LDH-3	125	72			~ 8	~ 15.8	130 ± 117

$(LDH/PSS)_n$	*LDH /wt.%*	*Platelet misalignment /°*	*LDH dep. Rate /abs.n⁻¹*	*PSS dep. Rate /abs.n⁻¹*
LDH-1	57.3	± 20	$4.84.10^{-4}$	$3.49.10^{-2}$
LDH-2	88.4	± 8	$1.21.10^{-3}$	$2.79.10^{-2}$
LDH-3	83.3	± 17	$1.91.10^{-3}$	$3.67.10^{-2}$

(S.D: standard deviation)

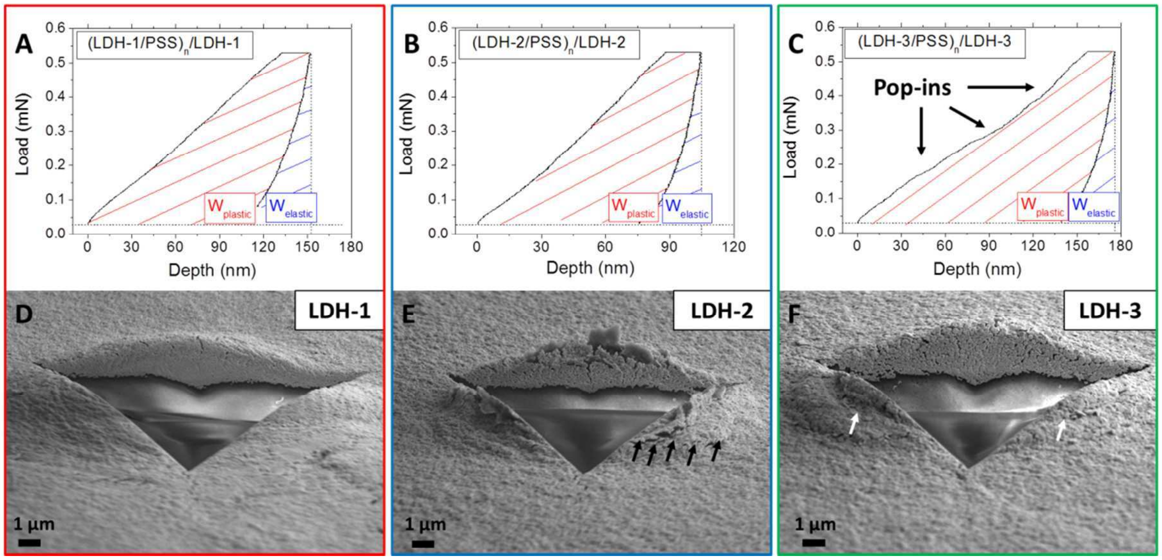

Figure 3. Mechanical properties of $(LDH/PSS)_n/LDH$ coating via nanoindentation. Load-displacement curves obtained from shallow nanoindentation of ~1.5 µm-thick $(LDH/PSS)_n/LDH$ coatings containing LDH-1 (n=200) (A), LDH-2 (n=75) (B), and LDH-3 (n=75) (C) platelets. SEM side view micrographs of *in-situ* indents made on (LDH-1/PSS)200/LDH-1 (D), (LDH-2/PSS)75/LDH-2 (E) and $(LDH\text{-}3/PSS)_{75/LDH\text{-}3}$ (F) ~1.5 µm-thick coating at a depth of 10 µm (black arrows indicate multiple and subsequent displacement of materials while white arrows point coating failures within the pileups).

The shape of the load-displacement curves relate to the active deformation mechanisms. The $(LDH\text{-}1/PSS)_n/LDH\text{-}1$ coatings show constant resistance to mechanical load as the predominantly organic matrix flows plastically. $(LDH\text{-}3/PSS)_n/LDH\text{-}3$ exhibits a high initial resistance to loading and subsequent softening evidenced by load drops ("pop-in") generated due to the presence of disorganized or unevenly sized inorganic platelets. For comparison, indentation of a geological aragonite monocrystal revealed the presence of "pop-ins" caused by stress accumulation underneath the indenter tip triggering catastrophic failure of the material; in contrast, natural nacre exhibits viscoelastic properties buffering stress concentrations within the platelets and yielding at a constant stress level.[2] The polydispersed randomly orientated platelets (LDH-3) do not allow for in-plane sliding of the platelets over one another as observed in natural nacre, even at high inorganic content (83.3 wt%). Instead, high local stress concentrations arise between the differently-sized platelets interface upon loading. Increasing the load applied to the coating eventually triggers failure of the jammed platelets, causing "pop-ins" in the loading segment of the load-displacement curve. In contrast, the $(LDH\text{-}2/PSS)_n/LDH\text{-}2$ coatings strain harden, an effect which can be attributed to in-plane sliding of the well-arranged LDH platelets and subsequent progressive platelet interlocking. This strain hardening phenomenon of $(LDH\text{-}2/PSS)_n/LDH\text{-}2$ coatings is similar to that of natural nacre,[47] although the exact mechanism of platelet interlocking is unclear; in natural systems, wedging,[55,56] asperities,[15,57] mineral bridges,[58,59] nanograin rotation[3] and negative Poisson's ratio[60] have been proposed.

Table 2. Mechanical properties of $(LDH/PSS)_n/LDH$ artificial nacre and standard errors

$(LDH/PSS)_n$	*Elastic modulus /GPa*	*Hardness /GPa*	*$W_{plastic}/W_{elastic}$*	*Platelet behavior*
LDH-1	*27.68 ± 0.98*	*1.35 ± 0.06*	*2.57 ± 0.05*	*Flow in matrix (movie S.1)*
LDH-2	*65.79 ± 3.16*	*2.34 ± 0.18*	*3.44 ± 0.13*	*Progressive interlocking (movie S.2)*
LDH-3	*35.30 ± 1.88*	*1.07 ± 0.12*	*3.20 ± 0.08*	*Failure (movie S.3)*

While quantitative values were extracted from the displacement-load curves obtained from indentation that were less than 15 % of coating thickness to avoid substrate effects, deeper indentations of about 10 µm were also performed in order to image the deformation mechanisms occurring in the vicinity of the indent directly in situ (Fig. 3.D-F). In all cases, the nanocomposite coatings were pushed aside and piled-up during deep indentation. $(LDH\text{-}1/PSS)_nLDH\text{-}1$, with its high organic content, exhibited large and even pileups at the edges of the indent with a blunted appearance, typical for a viscoelastic polymer, as observed for wet natural nacre.[61] The formation of smooth pileups indicates low friction within the coating and, therefore, no platelet interlocking. On the other hand, deep indentation into both $(LDH\text{-}2/PSS)_n/LDH\text{-}2$ and $(LDH\text{-}3/PSS)_n/LDH\text{-}3$, with their high inorganic contents, produced shorter, steeper pileups, indicating more friction in the coating during material rearrangement. This phenomenon has also been observed for dry natural nacre,[61] which exhibits more friction resistance at the platelet interface and greater strain hardening in its dry state.[62] These pileups show distinct features compared to the $(LDH\text{-}1/PSS)_n/LDH\text{-}1$ indents, which can be attributed to platelet interlocks and coating fracture in $(LDH\text{-}2/PSS)_n/LDH\text{-}2$ and $(LDH\text{-}3/PSS)_n/LDH\text{-}3$, respectively. The different origin of these features becomes clear when viewing the in situ nanoindentation videos (Movie S1-S3). Progressive hardening occurs in the coating containing LDH-2 platelets (Movie S2); the first wave of material pushed aside by the tip is arrested, leading to the initiation of secondary propagating waves within the pileups. The top-view of the $(LDH\text{-}2/PSS)_nLDH\text{-}2$ coatings after indentation (Fig. 4A), confirms multiple sites of platelet sliding within the pileups; a similar view of $(LDH\text{-}3/PSS)_n/LDH\text{-}3$ shows a more brittle deformation with cracks appearing in the hybrid material (Fig. 4B) presumably caused by stress accumulation at heterogeneities within the structure. Indeed, $(LDH\text{-}2/PSS)_n/LDH\text{-}2$ exhibits a higher ratio of plastic work (yielding) to elastic work compared to $(LDH\text{-}3/PSS)_n/LDH\text{-}3$ (Tab. 2), while maintaining a better integrity after deformation. Sliding and interlocking of a large number of platelets, within the well-organized $(LDH\text{-}2/PSS)_n/LDH\text{-}2$ nanostructure, can provide a mechanism for substantial plastic deformation, at high loadings, leading to a large work of deformation, combined with high modulus and hardness.

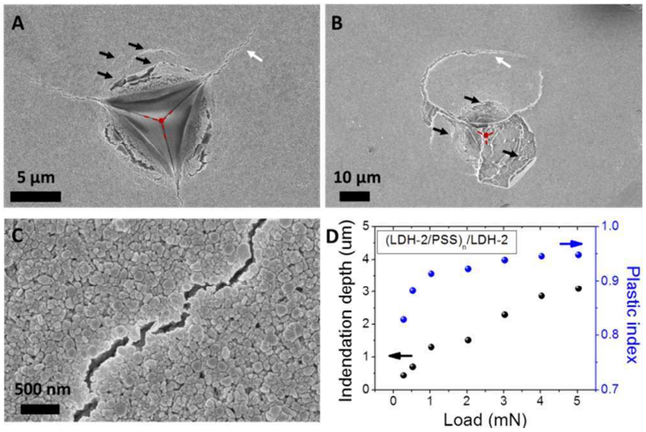

Figure 4. Ductile behaviour of $(LDH/PSS)_n/LDH$ coatings. Top view SEM images of indents made with a Berkovich tip into 1.5 µm-thick $(LDH\text{-}2/PSS)_n/LDH\text{-}2$ and $(LDH\text{-}3/PSS)_n/LDH\text{-}3$ (A and B, respectively) coatings at a depth of 5 µm (indents center are marked in red - black arrows evidence displacement of material within the pileups, while white arrows show cracks propagating from the indent). Top view SEM image show a crack propagating in $(LDH\text{-}2/PSS)_n/LDH\text{-}2$ coating (C). The plastic index of $(LDH\text{-}2/PSS)_n/LDH\text{-}2$ coating was measured from nanoindentation carried out at varying loads and depth (D).

In principle, fracture toughness can be estimated from the length of cracks triggered from the corners of indentations.[63] However, since the lengths of the cracks in the $(LDH/PSS)_n/LDH$ systems are short compared to the indent size, quantitative analysis is not valid (Fig. S8, supplementary information). Nevertheless, the much shorter cracks observed for $(LDH\text{-}2/PSS)_n/LDH\text{-}2$ compared to $(LDH\text{-}3/PSS)_n/LDH\text{-}3$ (7 and 70 µm, respectively), qualitatively indicate a much higher toughness (Fig. 4A and 4B). The short cracks initiated in $(LDH\text{-}2/PSS)_n/LDH\text{-}2$ coatings displayed significant deflections similarly to natural nacre[9,52] (Fig. 4C), whereas in $(LDH\text{-}3/PSS)_n/LDH\text{-}3$, the unevenly-sized platelet interfaces caused obvious local coating failures (Fig. 4B).

In order to estimate the energy absorption within the artificial nacre nanostructure, the plastic index[64] was measured for $(LDH\text{-}2/PSS)_nLDH\text{-}2$ (Fig. 4D). A thick coating was loaded with a sharp tip at various loads, at multiple platelet depths, to measure its index of plasticity, based on the areas of plastic deformation and viscoelastic recovery region under the load-displacement curve (Fig. S8, supplementary information). A stabilized plastic index of about 0.95 was measured for the $(LDH\text{-}2/PSS)_n/LDH\text{-}2$ coating, which is significantly higher than that of natural nacre of 0.78 and 0.72, measured from shallow[64] and deep[51] nanoindentation, respectively. Other nanoindentation load-displacement curves reported for natural nacre have a lower proportion of plastic deformation[21,57] than the $(LDH\text{-}2/PSS)_n/LDH\text{-}2$ coating.

The plasticity of the well-ordered $(LDH\text{-}2/PSS)_n/LDH\text{-}2$ suggests that platelet sliding and subsequent interlocking in the vicinity of the crack tip are important enablers of energy dissipation though local deformation and crack deflection. $(LDH\text{-}3/PSS)_n/LDH\text{-}3$ has a similar volume density of interface, but is not sufficiently ordered to allow controlled platelet sliding leading to strain hardening.

Conclusions

The synthesis of LDH platelets via a hybrid co-precipitation/hydrothermal method produced stable colloidal suspensions of well-defined platelets with an interesting intermediate thickness between single crystal layers and conventional nacre platelets. These nanoplatelets proved suitable for the successful LbL assembly of an ordered and dense layered nanostructure, with significantly improved quality compared to structures prepared from thicker platelets via dip coating techniques. The use of platelets with a narrow size distribution and small absolute size, allowed the self-assembly of dense films, with high inorganic content (~90 wt%), and a large number of layers (50-150) with platelet misalignment as low as 8°. It may be that the smaller size of platelets allows a degree of reversibility during the assembly process, encouraging greater order and better packing. This system echoes the “brick-and-mortar” structure of nacre, with similar proportions and aspect ratios, but uniformly scaled down by more than one order of magnitude. The minimum thickness of an adsorbed polymer layer (1-2 nm) which can act as the soft interface, in turn defines the minimum platelet thickness (~15 nm) which can maintain a high inorganic content. Thus the current system based on platelets around this thickness may represent an optimum. The known toughening mechanisms of nacre, such as platelet sliding and interlocking, as well as three dimensional crack deflections, were also found to occur in this reduced length scale embodiment. The observation of these coordinated mechanisms both confirms and requires the successful preparation of well-ordered films with the correct inorganic-organic composition; controls using more polydispersed or incorrectly sized platelets do not generate the required architecture or phenomenology. The best coatings possessed an elastic modulus and hardness close to that of natural nacre and yet allowed for larger substantial plastic deformation to occur in the material upon loading. The combination of high strength and stiffness along with plastic deformation is a long standing goal of nanocomposite materials. The reduction in scale of the “brick-and-mortar” structure allows for an increase in the absolute interface density, potentially leading to a greater toughness, whilst retaining the strain hardening mechanisms of nacre. These robust well-arranged bio-inspired hybrid nanocomposites offer opportunities to manufacture lightweight coatings with excellent mechanical performance. The use of nanoscale platelets is of interest as they become insensitive to pre-existing flaws, maximizing their strength and, therefore, allowing an increase of their critical aspect ratio[17]. Interestingly, good properties were manifested without the need to introduce a secondary nanocomposite grain structure within the platelets. Moderate increases in lateral platelet size, whilst maintaining the optimum thickness and avoiding platelet fracture, would offer improved all round mechanical performance for the design of high performance nanocomposites[23].

Methods

Materials: Poly (sodium 4-styrene sulfonate) solution (PSS, M_w 70,000 30 wt.% in H_2O), $Mg(NO_3)_2.6H_2O$, $Al(NO_3)_3.9H2O$, NaOH and Na_2CO_3 were purchased from Sigma-Aldrich. Microscope quartz and glass slides used for LbL deposition were obtained from UQG Optics Ltd. and Fisher Scientific, respectively. Deionized water (15 MΩ.cm^{-1}), sulphuric acid (95 %) and hydrogen peroxide (50 wt.% in H_2O) were supplied from VWR.

Synthesis of Mg_2-Al-CO_3-LDH: A 10 ml metal salt solution containing 2 mM of $Mg(NO_3)_2.6H_2O$ and 1 mM $Al(NO_3)_3.9H_2O$ as well as a 40 ml basic solution containing 6 mM NaOH and 0.6 mM Na_2CO_3 were prepared separately. The metal salt solution was added to the basic solution in less than 5 s, under vigorous stirring, followed by further stirring (750 rpm) at room temperature for 20 min. The mixture was then centrifuged at 15,000 rpm for 15 min to retrieve the LDH slurry. Subsequently, the slurry was washed twice by re-dispersion in deionized water followed by bath sonication (75 W) for 5 min and finally centrifugation at 15,000 rpm for 15 min. After washing, the slurry was dispersed in 25 ml deionized water (0.4 wt%) via bath sonication and placed in an autoclave for hydrothermal treatment at 100°C for 4 h and 72 h and at 125°C for 72 h. The time and temperature of the hydrothermal treatment were selected to synthesize platelets with varying dimensions, as described in Table 1. The LDH solution was used within the first month after the synthesis to avoid possible re-aggregation; the quality of the dispersion appeared stable over this timeframe.

Solutions: After hydrothermal treatment, 25 ml LDH dispersion in water was further diluted with 20 ml of deionized water to obtain a LDH dispersion with a concentration of about 0.3 wt.% with a pH of 10. 3.35 ml of PSS was added to 1 L of deionized water to form a polyelectrolyte (PE) aqueous solution with a concentration of 0.1 wt.%. The pH of the PSS solution was then adjusted to 10 by the addition of 0.1 M NaOH.

Substrate preparation: Prior to LbL coating, the substrate was cleaned with piranha solution using a 3:1 mixture of sulphuric acid and hydrogen peroxide (50 wt.%) to eliminate impurities and organic particles present on its surface. Quartz and glass slides were immersed in the piranha solution for about an hour, heated to 100°C and subsequently rinsed in DI water multiple times. After treatment, the substrate was stored in a sealed jar filled with deionized water for a maximum of two weeks.

Layer-by-Layer assembly of $(LDH/PSS)_n$: In order to form a monolayer of LDH platelets, the negatively charged substrate (glass or quartz) was dipped into the dispersion containing 0.3 wt.% positively charged LDH at pH 10 (as synthesized) for 10 min. The slide was subsequently rinsed by immersion in water at pH 10 for 2 min after LDH deposition, consisting in two dips of 30 s in two different water tubes. The rinsing step was carried out to wash away excess particles weakly associated to the surface/meniscus after each deposition. To form (LDH/PSS) bilayers and multilayers, the charged glass substrate was alternately dipped into the LDH (0.3 wt.%) dispersion and PSS solution (0.1 wt.%) for 10 min each, interspersed by 2 min-rinsing steps in water after each deposition. The pH was kept constant at 10 throughout the entire process. To deposit thick (LDH/PSS) multilayers coatings ($n > 15$), a home-made automatic dipping robot was used. The procedure was exactly the same as described above. The substrate dipping and removing rates were fixed at about 0.4 $cm.s^{-1}$. After deposition of the last layer, the coating was rinsed and allowed to dry at room temperature overnight before characterization.

Instrumental analysis: Zeta potential (Zeta PALS, Brookhaven) measurements were performed to determine the surface charge of LDH platelets while in suspension in KCl (5 mM) solution as a function of the pH (from 4 to 10). The dimensions and size distribution of the LDH platelets were measured by analyzing bright field transmission electron microscope (JEOL, 2000FX) images. The Layer-by-Layer assembly on quartz slides was monitored by UV-Vis spectroscopy (Lambda 35, PerkinElmer). Spectra were acquired over a wavelength range of 800 to 200 nm for samples containing different numbers of (LDH/PSS) bilayers. The absorption at 225 nm caused by the phenyl group of PSS was plotted as a function of the number of bilayers in the multilayer coating to confirm repeatable Layer-by-Layer deposition of each bilayer through linear fitting of the data. Reference spectra were acquired on cleaned quartz substrates without any coating. Coating roughness, as well as the deposition of the first LDH monolayer on quartz, was investigated by atomic force microscopy (Multimode 8, Bruker) in tapping mode. Imaging of the monolayer and multilayer coatings was performed on a scanning electron microscope (SEM, LEO Gemini 1525

FEGSEM). Due to the non-conductive nature of the layers, a thin layer of gold (5 to 10 nm) was sputter coated on top of each sample prior to imaging. SEM was used to image top surfaces and cross sections of the coatings, operating at 5 keV. The amount of LDH platelets in the coatings was determined using thermo-gravimetric analysis (Q500, TA Instruments). TGA was performed from 30°C to 900°C at a rate of 5°C/min in air (60 ml/min). Sample weights of 1.5 to 2.5 mg were used. In addition to the $(LDH/PSS)_n/LDH$ coatings, individual constituents of the multilayer such as PSS and LDH powders were also analyzed under the same conditions. The weight proportion of inorganic LDH was determined using a rule of mixtures. Sample cross-sections, less than 100 nm-thick were prepared by milling, using a gallium ion beam on a dual-beam focused ion beam (Nanolab 600, Helios). Prior to imaging under the FIB, the coating was first sputter coated with a thin layer of chromium (5 to 10 nm). A platinum rectangular layer (10*2 µm) of few micrometer-thick was deposited onto the coating using electron beam to prevent damage of the cross-section sample from gallium beam exposure of the top surface. Regular trenches were then milled from the coating at a FIB current of 21 nA on each sides of the platinum rectangle to form a thin lamella. After milling, platinum was deposited over a needle in contact with the lamella so that to lift up and transfer the lamella onto a TEM grid. Finally, the lamella was thinned down to a thickness of about 100 nm using a FIB current of 93 pA. A high-resolution transmission electron microscope (2100 FX, JEOL) equipped with an EDX spectrometer (20 KeV) was used to image and characterize the composition of the sample cross-section. XRD (X'Pert PRO, PANalytical) of LDH powders was carried out to determine the crystalline structure of the platelets using a Cu-Kα X-ray source (1.5418 Å). Diffractograms of $(LDH/PSS)_n/LDH$ coatings were also acquired to assess the presence of LDH and organic content without any other contamination. Three-dimensional rocking curves were measured on $(LDH/PSS)_n/LDH$ coatings to determine the alignment of the platelets within the nacre-like coating. 2θ was fixed at 11.7° to investigate the diffraction of the (003) crystallographic plane of the platelets, which is expected to be parallel to the surface of the substrate in a well ordered system. Ψ (tilt angle) was increased from 0 to 80° in 5° steps. For each value of Ψ, diffraction intensity was recorded during a full revolution (Φ) of the sample around each value of Ψ with a step of 5° to investigate the misalignment of the platelets in all directions. The mechanical properties of the $(LDH/PSS)_n/LDH$ coatings were investigated using nanoindentation (Nanotest NTX, Micro Materials) equipped with a Berkovich tip with a pyramidal shape and the Oliver and Pharr method.[48] The coatings were indented 36 times with a spacing of 100 µm between the indents along both the X and Y axis at room temperature. Indent depth was limited to the first 15 % of the coating thickness to avoid any substrate effect while applying a load of 300 µN within 30 s. Viscoelasticity of the coatings through deformation of the polymer phase was investigated by holding the indentation maximum load for about 30 s allowing the coating to creep. Unloading of the coatings was carried out within 30 s. Large and deep indents on 1.5 µm-thick coatings were achieved applying large loads in the range of 150 and 500 mN, which led to an indentation depth of about 5 and 10 µm, respectively. Nanoindentation was carried out in situ within an SEM (Auriga, Carl Zeiss) with a cube-corner tip to investigate the deformation mechanism of the nanostructures. Plastic deformation of $(LDH\text{-}2/PSS)_n/LDH$ was investigated *via* nanoindentation while loading a 3.5 µm-thick coating with a cube-corner tip at varying loads (0.25 to 5 mN). The index of plasticity[64] was obtained from the equation below:

$$\xi = \frac{A_1}{A_1 + A_2}$$

Where A_1 and A_2 are the areas of the plastic deformation and viscoelastic recovery region under the load-displacement curve, respectively.

Acknowledgment

We thank R. Sweeney for help with the rocking curve experiment, C. Ware and M. Ardakani for help with the TEM cross-sections and finally F. Giuliani and G. Sernicola help with the SEM *in-situ* nanoindentation. We greatly acknowledge J. Elsdon for designing

and building the robotic-dipping LbL system used for this research.

SUPPORTING INFORMATION

Figures S1-S8 and Movies S1-S3, as described in the text. This material is available free of charge via the Internet at http://pubs.acs.org."

Corresponding Author

* Milo S. P. Shaffer
Email: m.shaffer@imperial.ac.uk.
Department of Chemistry, Imperial College London, South Kensington Campus, London SW7 2AZ, UK.

Present Addresses

† Jonny J. Blaker
Current address: Materials Science Centre, School of Materials, The University of Manchester, Grosvenor Street, Manchester M1 7HS, UK

Author Contributions

J.J.B. started the project with another type of nanoplatelet material using a LbL approach. J.B. developed the method to synthesize Mg$_2$-Al-CO$_3$-LDH nanoplatelets. R.M. helped with the synthesis of the nanoplatelets. F.D.L. produced and characterized the different LDH nanoplatelets, developed the LbL procedure and assembled the nanostructures. F.D.L. characterized the nanostructures morphology and mechanical properties. The project was supervised by M.S.P.S. and A.B. The manuscript was written by F.D.L. and M.S.P.S. with contributions from the other authors.

Funding Sources

This work was funded under the UK Engineering and Physical Sciences Research Council (EPSRC) Programme Grant EP/I02946X/1 on High Performance Ductile Composite Technology in collaboration with Imperial College, London. Supporting data are available, subject to a non-disclosure agreement. Please contact the corresponding author in the first instance.

References

1 Sen, D.; Buehler, M. J. Structural Hierarchies Define Toughness and Defect-tolerance Despite Simple and Mechanically Inferior Brittle Building Blocks. *Sci. Rep.* **2011**, 1, 35.
2 Huang, Z.; Li, X. Origin of Flaw-tolerance in Nacre. *Sci. Rep.* **2013**, 3, 1693.
3 Li, X.; Xu, Z.-H.; Wang, R. In Situ Observation of Nanograin Rotation and Deformation in Nacre. *Nano lett.* **2006**, 6 (10), 2301-2304.
4 Li, X.; Huang, Z. Unveiling the Formation Mechanism of Pseudo-Single-Crystal Aragonite Platelets in Nacre. *Phys. Rev. Lett.* **2009**, 102, 075502.
5 Rousseau, M.; Lopez, E.; Stempfle, P.; Brendle, M.; Franke, L.; Guette, A.; Bourrat, X. Multiscale Structure of Sheet Nacre. *Biomaterials* **2005**, 26 (31), 6254-6262.
6 Stempflé, P.; Pantalé, O.; Rousseau, M.; Lopez, E.; Bourrat, X. Mechanical Properties of the Elemental Nanocomponents of Nacre Structure. *Mater. Sci. Eng. C* **2010**, 30 (5), 715-721.
7 Shao, Y.; Zhao, H. P.; Feng, X. Q. On Flaw Tolerance of Nacre: A Theoretical Study. *J. R. Soc., Interface* **2014**, 11 (92), 20131016.
8 Fleischli, F. D.; Dietiker, M.; Borgia, C.; Spolenak, R. The Influence of Internal Length Scales on Mechanical Properties in Natural Nanocomposites: A Comparative Study on Inner Layers of Seashells. *Acta biomater.* **2008**, 4 (6), 1694-1706.
9 Meyers, M. A.; Lin, A. Y.; Chen, P. Y.; Muyco, J. Mechanical Strength of Abalone Nacre: Role of the Soft Organic Layer. *J. Mech. Behav. Biomed. Mater.* **2008**, 1 (1), 76-85.
10 Jackson, A. P.; Vincent, J. F. V.; Turner, R. M. The Mechanical Design of Nacre. *Proc. R. Soc. London, ser. B* **1988**, 234 (1277), 415-440.
11 Currey, J. D. Mechanical Properties of Mother of Pearl in Tension. *Proc. R. Soc. B* **1977**, 196 (1125), 443-463.
12 Katti, K. S.; Katti, D. R. Why is Nacre So Tough and Strong? *Mater. Sci. Eng. C* **2006**, 26 (8), 1317-1324.
13 Katti, K. S.; Katti, D. R.; Pradhan, S. M.; Bhosle, A. Platelet Interlocks are the Key to Toughness and Strength in Nacre. *J. Mater. Res.* **2011**, 20 (5), 1097-1100.
14 Espinosa, H. D.; Rim, J. E.; Barthelat, F.; Buehler, M. J. Merger of Structure and Material in Nacre and Bone – Perspectives on de Novo Biomimetic Materials. *Prog. Mater. Sci.* **2009**, 54 (8), 1059-1100.
15 Wang, R. Z.; Suo, Z.; Evans, A. G.; Yao, N.; Aksay, I. A. Deformation Mechanisms in Nacre. *J. Master. Res.* **2001**, 16 (9), 2485-2493.
16 Wang, R. Z.; Wen, H. B.; Cui, F. Z.; Zhang, H. B.; Li, H. D. Observations of Damage Morphologies in Nacre Deformation and Fracture. *J. Mater. Sci.* **1995**, 30 (9), 2299-2304.
17 Gao, H.; Ji, B.; Jager, I. L.; Arzt, E.; Fratzl, P. Materials Become Insensitive to Flaws at Nanoscale: Lessons from Nature. *Proc. Natl. Acad. Sci. U. S. A.* **2003**, 100 (10), 5597-5600.
18 Gao, H.; Ji, B.; Buehler, M. J.; Yao, H. Flaw Tolerant Bulk and Surface Nanostructures of Biological Systems. *Mech. Chem. Biosyst.* **2004**, 1 (1), 37-52.
19 Wang, R.; Gupta, H. S. Deformation and Fracture Mechanisms of Bone and Nacre. *Annu. Rev. Mater. Res.* **2011**, 41, 41-73.
20 Meyers, M. A.; Chen, P.-Y.; Lin, A. Y.-M.; Seki, Y. Biological Materials: Structure and Mechanical Properties. *Prog. Mater. Sci.* **2008**, 53, 1-206.
21 Li, X.; Chang, W.; Chao, Y.; Wang, R.; Chang, M. Nanoscale Structural and Mechanical Characterization of a Natural Nanocomposite Material: The Shell of Ref Abalone. *Nano lett.* **2004**, 4 (4), 613-617 .
22 Barthelat, F.; Rabiei, R. Toughness Amplification in Natural Composites. *J. Mech. Phys. Solids* **2011**, 59 (4), 829-840.
23 Bekah, S.; Rabiei, R.; Barthelat, F. Structure, Scaling, and Performance of Natural Micro- and Nanocomposites. *Bionanosci.* **2011**, 1 (1), 53-61.
24 Barthelat, F. Designing Nacre-like Materials for Simultaneous Stiffness, Strength and Toughness:

Optimum Materials, Composition, Microstructure and Size. *J. Mech. Phys. Solids* **2014**, 73 , 22-37.

25 Wang, J.; Cheng, Q.; Tang, Z. Layered Nanocomposites Inspired by the Structure and Mechanical Properties of Nacre. *Chem. Soc. Reviews* **2012**, 41, 1111-1129.

26 Bonderer, L. J.; Studart, A. R.; Gauckler, L. J. Bioinspired Design and Assembly of Platelet Reinforced Polymer Films. *Science* **2008**, 319 (5866), 1069-1073.

27 Yao, H. B.; Ge, J.; Mao, L. B.; Yan, Y. X.; Yu, S. H. 25th Anniversary Article: Artificial Carbonate Nanocrystals and Layered Structural Nanocomposites Inspired by Nacre: Synthesis, Fabrication and Applications. *Adv. Mater.* **2014**, 26 (1), 163-187.

28 Cheng, Q.; Jiang, L.; Tang, Z. Bioinspired Layered Materials with Superior Mechanical Performance. *Acc. Chem. Res.* **2014**, 47 (4), 1256-1266.

29 Yao, H. B.; Fang, H. Y.; Tan, Z. H.; Wu, L. H.; Yu, S. H. Biologically Inspired, Strong, Transparent, and Functional Layered Organic-inorganic Hybrid Films. *Angew. Chemie* **2010**, 122, 2186-2191.

30 Shu, Y.; Yin, P.; Wang, J.; Liang, B.; Wang, H.; Guo, L. Bioinspired Nacre-like Heparin/Layered Double Hydroxide Film with Superior Mechanical, Fire-Shielding, and UV-Blocking Properties. *Ind. Eng. Chem. Res.* **2014**, 53 (10), 3820-3826.

31 Tang, Z.; Kotov, N. A.; Magonov, S.; Ozturk, B. Nanostructured Artificial Nacre. *Nat. Mater.* **2003**, 2, 413-418.

32 Yao, H. B.; Tan, Z. H.; Fang, H. Y.; Yu, S. H. Artificial Nacre-like Bionanocomposite Films from the Self-assembly of Chitosan-montmorillonite Hybrid Building Blocks. *Angew. Chemie* **2010**, 49 (52), 10127-10131.

33 Walther, A.; Bjurhager, I.; Malho, J-M.; Pere, J.; Ruokolainen, J.; Berglund, L. A.; Ikkala, *O.* Large-area, Lightweight and Thick Biomimetic Composites with Superior Material Properties via Fast, Economic, and Green Pathways. *Nano Lett.* **2010**, 10 (8), 2742-2748.

34 Wang, J.; Cheng, Q.; Lin, L.; Jiang, L. Synergistic Toughening of Bioinspired Poly(vinyl alcohol)-Clay-Nanofibrillar Cellulose Artificial Nacre. *ACS Nano* **2014**, 8 (3), 2739-2745.

35 Das, P.; Malho, J-M.; Rahimi, K..; Schacher, G. H.; Wang, B.; Demco, D. E.; Walther, A. Nacre-mimetics with Synthetic Nanoclays Up to Ultrahigh Aspect Ratios. *Nat. commun.* **2015**, 6, 5967.

36 Tan, Z.; Zhang, M.; Li, C;, Yu, S.; Shi, G. A General Route to Robust Nacre-Like Graphene Oxide Films. *ACS Appl. Mater. Interfaces* **2015**, 7 (27), 15010-15016.

37 Li, Y. Q.; Yu, T.; Yang, T. Y.; Zheng, L. X.; Liao, K. Bio-inspired Nacre-like Composite Films Based on Graphene with Superior Mechanical, Electrical, and Biocompatible Properties. *Adv. Mater.* **2012**, 24, 3426-3431.

38 Cheng, Q.; Wu, M.; Li, M.; Jiang, L.; Tang, Z. Ultratough Artificial Nacre Based on Conjugated Cross-linked Graphene Oxide. *Angew. Chemie* **2013***,* 125 (13) , 3838-3843.

39 Putz, K. W.; Compton, O. C.; Palmeri, M. J.; Nguyen, S. T.; Brinson, L. C. High-Nanofiller-Content Graphene Oxide-Polymer Nanocomposites via Vacuum-Assisted Self-Assembly. *Adv. Funct. Mater.* **2010**, 20 (19), 3322-3329.

40 Cui, W.; Li, M.; Liu, J.; Wang, B.; Zhang, C.; Jiang, L.; Cheng, Q. A Strong Integrated Strength and Toughness Artificial Nacre Based on Dopamine Cross-Linked Graphene Oxide. *ACS Nano* **2014**, 8 (9), 9511-9517.

41 Zhang, M.; Huang, L.; Chen, J.; Li, C.; Shi, G. Ultratough, Ultrastrong, and Highly Conductive Graphene Films with Arbitrary Sizes. *Adv. Mater.* **2014**, 26 (45), 7588-7592.

42 Wang, J.; Cheng, Q.; Lin, L.; Chen, L.; Jiang, L. Understanding the Relationship of Performance with Nanofiller Content in the Biomimetic Layered Nanocomposites. *Nanoscale* **2013**, 5, 6356-6362.

43 Kotov, N. A. Ordered Layered Assemblies of Nanoparticles. *MRS Bull.* **2001**, 26 (12), 992-997.

44 Xu, Z. P.; Stevenson, G.; Lu, C.-Q.; Lu, G. Q. Dispersion and Size Control of Layered Double Hydroxide Nanoparticles in Aqueous Solutions. *J. Phys. Chem. B* **2006**, 110 (34), 16923-16929.

45 Unsworth, N. K.; Hancox, I.; Dearden, A.; Sullivan, P.; Walker, M.; Lilley, R. S.; Sharp, J.; Jones, T. S. Comparison of Dimethyl Sulfoxide Treated Highly Conductive Poly(3,4-ethylenedioxythiophene):poly(styrenesulfonate) Electrodes for Use in Indium Tin Oxide-free Organic Electronic Photovoltaic Devices. *Org. Electron.* **2014**, 15 (10), 2624-2631.

46 Masuda, K..; Abe, T.; Benten, H.; Ohkita, H.; Ito, S. Fabrication and Conductive Properties of Multilayered Ultrathin Films Designed by Layer-by-Layer Assembly of Water-soluble Fullerenes. *Langmuir* **2010**, 26 (16), 13472-13478.

47 Sun, J.; Bhushan, B. Hierarchical Structure and Mechanical Properties of Nacre: A Review. *RSC Adv.* **2012**, 2, 7617-7632.

48 Oliver, W. C.; Pharr, G. M. An Improved Technique for Determining Hardness and Elastic Modulus Using Load and Displacement Sensing Indentation Experiments. *J. Mater. Res.* **1992**, **7** (6), 1564-1583.

49 Finnemore, A.; Cunha, P.; Shean, T.; Vignolini, S.; Guldin, S.; Oyen, M.; Steiner, U. Biomimetic Layer-by-Layer Assembly of Artificial Nacre. Nat. Commun. ***2012,*** 3, 966.

50 Shu, Y.; Yin, P.; Liang, B.; Wang, S.; Gao, L.; Wang, H.; Guo, L. Layer by Layer Assembly of Heparin/Layered Double Hydroxide Completely Renewable Ultrathin Films with Enhanced Strength and Blood Compatibility. J Mater. Chem. **2012***,* 22, 21667-21672.

51 Katti, K. S.; Mohanty, B. ; Katti, D. R. Nanomechanical Properties of Nacre. J. Mater. Res. **2011**, 21, 1237-1242.

52 Leung, H. M.; Sinha, S. K. Scratch and Indentation Tests on Seashells. *Tribology Inter.* **2009**, 42, 40-49.

53 Sun, J.; Ling, M.; Wang, Y.; Chen, D.; Zhang, S.; Tong, J.; Wang, S. Quasi-Static and Dynamic Nanoindentation of Some Selected Biomaterials. *J. Bionic Eng.* **2014**, 11 (1), 144-150.

54 Burghard, Z.; Zini, L.; Srot, V.; Bellina, P.; Bill, J. Toughening through Nature-Adapted Nanoscale Des ign. Nano lett. **2009**, 9, 4103-4108.

55 Barthelat, F. Nacre from Mollusk Shells: A Model for High-performance Structural Materials. *Bioinspiration Biomimetics* **2010**, 5, 1-8.

56 Barthelat, F.; Espinosa, H. D. An Experimental Investigation of Deformation and Fracture of Nacre–Mother of Pearl. *Exp. Mech.* **2007**, 47, 311-324.

57 Barthelat, F.; Li, C. M.; Comi, C.; Espinosa, H. D. Mechanical Properties of Nacre Constituents and their Impact on Mechanical Performance. *J. Mater. Res.* **2006**, 21 (08), 1977-1986.

58 Song, F.; Soh, A. K.; Bai, Y. L. Structural and Mechanical Properties of the Organic Matrix Layers of Nacre. *Biomaterials* **2003**, 24 (20), 3623-3631.

59 Song, F.; Bai, Y. L. Effects of Nanostructures on the Fracture Strength of the Interfaces in Nacre. *J. Master. Res.* **2003**, 18 (08), 1741-1744.

60 Espinosa, H. D.; Juster, A. L.; Latourte, F. J.; Loh, O. Y.; Gregoire, D.; Zavattieri, P. D. Tablet-level Origin of Toughening in Abalone Shells and Translation to Synthetic Composite Materials. *Nat. Commun.* **2011**, 2, 173.

61 Bezares, J.; Asaro, R. J.; Zhangli, P.; Zhu, Q. Macromolecular Structure and Viscoelastic Response of the Organic Framework of Nacre in Haliotis Rufescens: A Perspective and Overview. *Theroret. Appl. Mech.* **2001**, 38, 75-106.

62 Barthelat, F.; Tang, H.; Zavattieri, P.; Li, C.; Espinosa, H. On the Mechanics of Mother-of-pearl: A Key Feature in the Material Hierarchical Structure. *J. Mech. Phys. Solids* **2007**, 55 (2), 306-337.

63 Ostojic, P.; McPherson, R. A Review of Indentation Fracture Theory: Its Development, Principles and Limitations. *Int. J. of Fract.* **1986**, 33, 297-312.

64 Sun, J.-y.; Tong, J. Fracture Toughness Properties of Three Different Biomaterials Measured by Nanoindentation. *J. Bionic Eng.* **2007**, 4 (1), 11-17.